IDENTIFICATION OF LINEAMENTS WITH POSSIBLE STRUCTURAL ORIGIN USING ASTER IMAGES AND DEM DERIVED PRODUCTS IN WESTERN CRETE, GREECE

Eirini S. Papadaki[1], Stelios P. Mertikas[1], and Apostolos Sarris[2]

1. Technical University of Crete, Department of Mineral Resources Engineering, Chania (Crete), Greece; eipapadaki(at)isc.tuc.gr
2. Foundation for Research & Technology (FORTH), Institute for Mediterranean Studies, Rethymno (Crete), Greece

ABSTRACT

The application of remote sensing technology, over more than three decades, has shown a great promise for large-scale geological mapping. This work presents an investigation for enhancing lineaments with possible relevance to faults, in Western Crete, Greece using a multi-spectral ASTER satellite image and standard geographic information systems (GIS) techniques. Image processing involved: a) the Principal Component Analysis; b) the computation of the normalized vegetation index image; and c) the generation of False Colour Composite images. The capability of the ASTER thermal infrared (TIR) bands to detect lineaments that might be related to failure of the crust has been evaluated. Moreover, a digital elevation model has been used to create the shaded relief and maps for the slope and aspect of the terrain. Remote sensing results have been compared, in digital form, with the drainage network at a scale of 1:50 000 and geological maps at scales of 1:200 000 and 1:50 000. Lineaments related to steep slopes, straight valley segments, abrupt changes in vegetation coverage and sudden bends along river courses have been evaluated as potential faults. Fieldwork surveys have been carried out in selected regions of interest. The applied methodology has contributed in identifying several known large-scale faults in Western Crete, Greece and mapping their potential extension.

INTRODUCTION

Fault detection is an essential element in the field of structural, economic and environmental geology (1,2). Traditional methods of mapping faults require fieldwork investigations. However, fieldwork is usually time consuming and may take up years to complete, depending primarily on the extension and/or the accessibility of the area under investigation (3). Topography, erosion, overgrowth of vegetation, scale, experience of the geologist and other factors control fault determination in the field.

On the other hand, remote sensing has the advantage of providing synoptic overviews of the region; thus it may directly pinpoint the characteristics of structural geological features extending over large areas (2). As opposed to fieldwork investigations, remote sensing along with image processing techniques accounts for a less time-consuming and a more cost-effective method for fault detection. Nonetheless, such techniques in no way replace field investigations, but on the contrary they complement each other.

Faults are often revealed as linear or curvilinear traces on satellite images. These image lines of different contrast are commonly referred to as lineaments (4) and may extend from a few metres to tens of kilometres in length. Certainly not all lineaments relate to faulting. They could also be attributed to lithological boundaries, boundaries between different land uses, drainage lines or even to man-made constructions such as roads. Therefore, it is not easy to interpret the potential structural origin of lineaments based on satellite images only. Furthermore, any vertical ground displacement accompanying failure of the crust cannot be easily detected on satellite images because of their planar view.

On the other hand, a fault plane may offer a preferred avenue to moisture, or vegetative growth, and may form specific drainage patterns easily detected on satellite images. More particularly, streams have a natural tendency to meander. Thus some frequently-found types of stream anomalies, such as straight segments, sudden bends observed along stream courses, displacement or even local disappearance of drainage system into lines of sinkholes could mark a fault line on an image (2,5). In addition, groundwater transferred through faults increases the moisture content of soil in relation to the surrounding area and promotes preferential alignments of vegetation, abrupt changes in vegetation canopy and sudden disappearance of a certain plant species (5).

Previous investigations have proposed various processing techniques for fault detection on multi-spectral images. Nama (6) applied a Principal Component Analysis on Landsat Enhanced Thematic Mapper imagery (ETM+) and managed to reveal the extent of the deformation caused during the volcanic eruptions in 1999 on Mount Cameroon, Cameroon. Ali *et al.* in (7) demonstrated that tectonic structures in south-west Iran could be delineated through contrast stretching of Landsat 7-ETM Band 4 in combination to the application of directional filters and the generation of different combinations of False Colour Composites. Similarly, Kenea (8), Suzen and Toprak (9), and Heddi *et al.* (10) showed that the combination of different processing techniques (for example the Principal Component Analysis, the creation of False Colour Composite images and the intensity-hue-saturation transformation), may contribute in geology and fault mapping. Recent investigations on lineament mapping using multi-spectral imagery may be found in (11-13).

In this paper, a multi-spectral ASTER (Advanced Spaceborne Thermal Emission and Reflection Radiometer) satellite image has been processed to enhance lineaments which are potential faults in Western Crete, Greece. No ASTER imagery has been used in the past for a geological application in the area of interest.

Compared to Landsat and SPOT imagery that have already been successfully used for geological applications in Crete (14-16), ASTER covers a wider spectral region. It contains 14 spectral bands from the visible to the thermal infrared (17). Its spatial resolution varies with wavelength, from 15 m × 15 m in the visible and near-infrared (VNIR), to 30 m × 30 m in the short wave infrared (SWIR) and finally to 90 m × 90 m in the thermal infrared (TIR) bands. In addition, the ASTER TIR bands allow retrieval of both surface temperature and spectral emissivity properties. These parameters can be used in a wide variety of activities, such as environmental monitoring, geological mapping and hazard prediction. As will be presented later on, a preliminary approach investigated the appropriateness of the TIR bands of ASTER for lineament detection.

GEOLOGICAL SETTING OF THE AREA

The location of Crete in the centre of the east Mediterranean Sea has a direct effect on the island's climate. It is characterised as temperate Mediterranean locus. Winter is mild, while summer is quite hot and arid. The mountain ranges are mostly rugged. The White Mountain range, being the backbone of West Crete, spans in a west to east direction with maximum altitude of 2453 m. Generally, the island of Crete is a densely vegetated area with olive trees, oaks, woods, scrubs and vineyards, making both field campaigns and remote sensing techniques for geological investigations quite difficult.

The geology of Crete is rather complicated because of the geotectonic location of the island in relation to the two lithospheric plates of Africa and Eurasia (Figure 1a). Crete comprises a pile of nappes derived from different paleogeographic zones. These nappes are divided into two major groups; the upper nappes and the lower nappes, separated by a major normal detachment fault (18).

Three individual groups constitute the lower nappes (Figure 1b): 1) the Plattenkalk unit which is the lowermost unit composed of Permian to Oligocene metacarbonate rocks; 2) the Trypali nappe, which lies tectonically over the Plattenkalk unit in western Crete and consists of carbonate, recrystallized conglomerates, limestones and dolomites of Triassic to Lower Jurassic age (19); and 3) the Phyllite-Quartzite unit. The latter one is the shallowest Late Carboniferous to Late Triassic package of sedimentary rocks, composed mostly of quartz-rich siliciclastic sediments, with minor limestone, gypsum and volcanic rocks (20). These pre-alpine units were affected by a high-pressure–low-temperature metamorphism in the late Oligocene to early Miocene. Today, they form the footwall of

a major low-angle normal fault or extensional detachment fault of lower to middle Miocene age. This zone of crustal detachment separates the lower, high-pressure–low-temperature units from the upper, alpine nappes, i.e., the Tripolitza and the Pindos units (21-23).
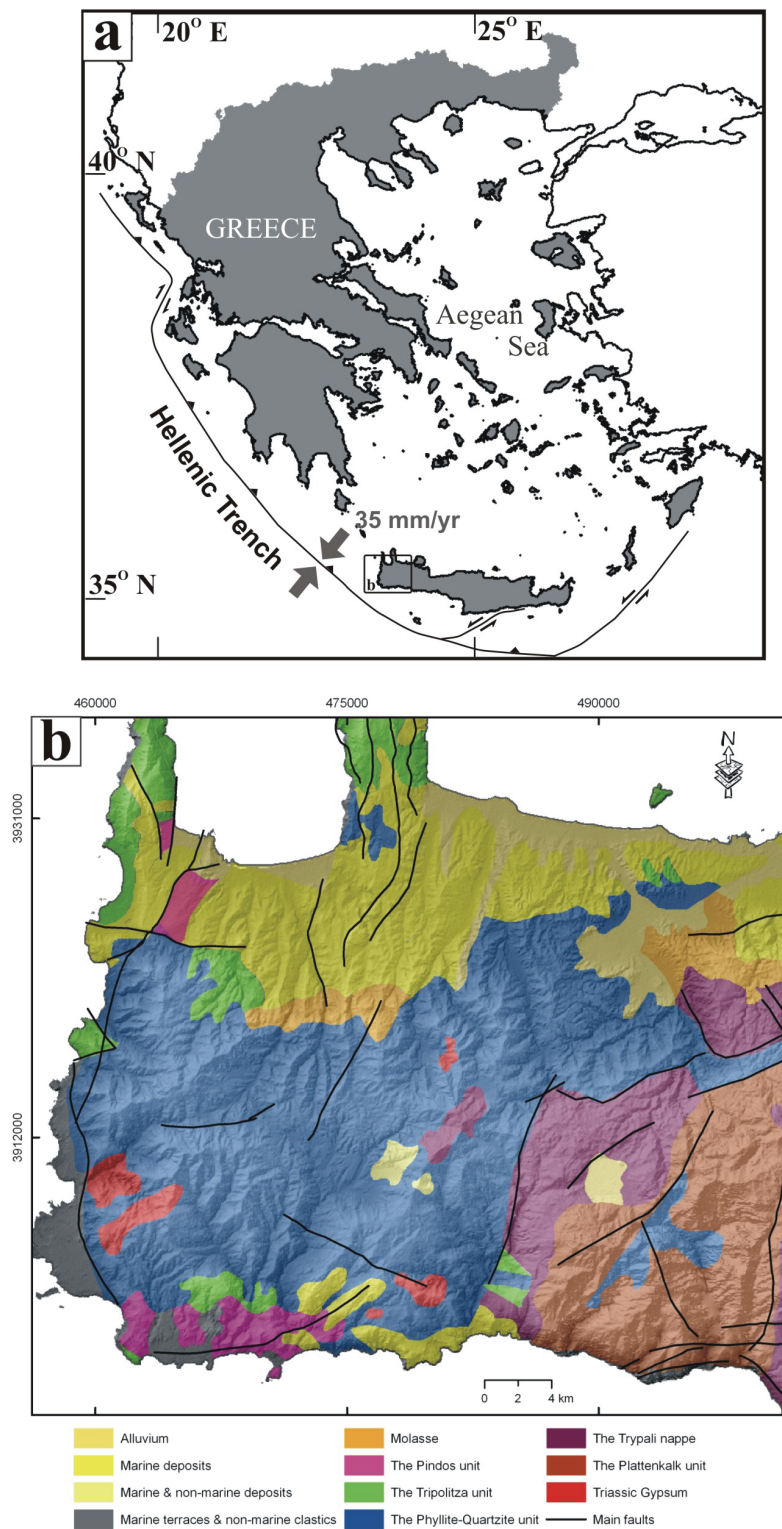

Figure 1: (a) General map showing the geographical location of the study area (inset) with respect to Greece and the Hellenic Arc. The rate of subsidence of the Eurasian Plate under the African Plate amounts to about 4cm/yr. (b) Geological map of West Crete (Institute of Geology and Mineral Exploration, IGME, scale 1: 200 000) showing the main geological formations and faults. The map is referenced to the Greek Geodetic Reference System of 1987 (in metres). A slight transparency shows the elevation model in the background.

The Pindos unit is mainly composed of Cretaceous flysch of Upper Cretaceous to Paleocene - Lower Eocene pelagic limestones, while the Tripolitza unitmainly includes Jurassic to Eocene grey limestones and dolomites. The basins of the area (Figure 1b) are half-graben structures filled by huge masses of clastic sediments (breccio-conglomerates) exclusively derived from the Tripolitza and Pindos units. Those are situated on top of the detachment fault (24) and are in turn overlain by marine strata of upper Miocene age (25).

Crete is a complex multi-fractured macrostructure characterized by geological faults mainly aligning along the North-South and East-West direction. Inside these first-order macrostructures, a considerable number of small order structures are also present. A more extensive review of the geological setting of the west Crete area under investigation is provided by (26) and (27).

METHODOLOGY

The methodology presented in this paper for the identification of lineaments with possible structural origin has been divided into three implementation phases:

    a. Image processing for the enhancement and digitizing of lineaments in West Crete using a multi-spectral ASTER level-1B (L1B) product. Emphasis has been given to large-scale lineaments that might have relevance with specific geomorphology and drainage patterns commonly related to faults.

    b. Processing of the Digital Elevation Model of the area.

    c. Setting up procedures through a Geographic Information System (GIS) for the evaluation of the lineaments detected on ASTER, as potential faults.

Image processing

The satellite image processed was a geolocated and radiometrically accurate radiance at sensor product (L1B) with Granule ID: SC:AST_L1B.003:2007878534 [1]. The image was acquired on 4 June 2002 (day-time acquisition) and covers an area in west Crete of 60km×60km having its scene centre located at 35º29' latitude (North) and 23º55' longitude (East). The data were geocoded to the World Geodetic System (WGS84) and its associated Universal Transverse Mercator projection.

At the first phase, atmospheric corrections have been applied separately on the VNIR and the SWIR channels. Reductions have been based on the so-called 'dark object subtraction' or 'the minimum band value' method (28). In this case, the assumption is that in near and short-wave infrared, clear and deep water return practically no radiation to the sensor in this band. Therefore, if the digital number value for these image areas is greater than zero, that value represents atmospheric interference contribution. By subtracting this value from each individual pixel in the band, a first-order atmospheric correction may be accomplished. Other more complicated and obviously precise atmospheric correction techniques can be also applied (28).

Despite the coarse spatial resolution of the ASTER TIR bands, their usefulness in lineament detection has been examined. As mentioned in the introduction, groundwater, often finds easy passage through fault zones, and therefore increases moisture in soil. Consequently, linear or curvilinear patterns of soil moisture content on a satellite image might be an index of failure of the crust. Particularly thermal imagery brings out the differential soil moisture content by virtue of temperature variations. This is justified by the fact that water in moist soils tends to keep them cooler than drier soils during day and night time. As a result, greyscale TIR images show darker patterns where the amount of moisture is higher (http://rst.gsfc.nasa.gov/).

The ASTER L1B-TIR data that were available for this study correspond to radiant temperature values (i.e., at-sensor temperature values). Retrieval of actual surface radiance as well as emissivity and temperature characteristics from the TIR radiance-at-sensor values could be achieved after removing the atmospheric interference from them. Such algorithms for atmospheric reductions are usually based on calculating the radiative transfer, using for example the MODTRAN code, com-

---

[1] see https://lpdaac.usgs.gov/lpdaac/products/aster_products_table for ASTER products

bined with atmospheric profiles from a numerical forecast system (29), or separating the temperature from the emissivity properties of earth targets (30). However, the application of precise atmospheric reduction techniques was beyond the scope of this work. In a rather generalized approach, TIR band analysis has been based on the fact that dark pixels on a greyscale TIR image relate to targets of low radiant temperature. Along these lines, the aim was to detect dark linear or curvilinear features that might suggest increased soil moisture content and therefore potential fracturing.

Pre-processing in the case of the five TIR bands, has involved masking the unwanted signal coming from the sea. Further, because of subtle inter-telescope mismatch (31), the SWIR and TIR data were registered and resampled to the VNIR by using ground control points. All 14 ASTER bands were then reduced to the Greek Geodetic Reference System 1987 (GGRS87) and referenced to the associated Transverse Mercator projection (32).

Image processing for lineament detection has been performed on the basis of enhancing potential soil moisture concentration and vegetation patterns. Image processing techniques involved: a) the Principal Component Analysis; b) the computation of the normalized vegetation index image; and c) the generation of False Colour Composite images.

Principal Component Analysis

Processing of 14 image bands may become cumbersome and time-consuming. The aim of the Principal Component Analysis (PCA) has been to compute inter-band correlations (Table 1) and to compress spectral information from the 14 original bands to less, but more useful uncorrelated images.

Table 1: Inter-band correlations between the 14 original ASTER bands.

	Visible-green	Visible-red	Near-infrared	SWIR	SWIR	SWIR	SWIR	SWIR	SWIR	TIR	TIR	TIR	TIR	TIR
	Band1	Band2	Band3N	Band4	Band5	Band6	Band7	Band8	Band9	Band10	Band11	Band12	Band13	Band14
Band1	1	0.976	0.089	0.772	0.804	0.813	0.813	0.815	0.749	0.370	0.373	0.368	0.385	0.365
Band2	0.976	1	0.047	0.790	0.818	0.829	0.827	0.831	0.762	0.404	0.407	0.402	0.418	0.399
Band3N	0.089	0.047	1	0.221	0.092	0.087	0.052	0.044	0.002	0.188	0.193	0.198	0.171	0.178
Band4	0.772	0.790	0.221	1	0.954	0.962	0.948	0.928	0.846	0.553	0.558	0.562	0.544	0.525
Band5	0.804	0.818	0.092	0.954	1	0.986	0.979	0.972	0.919	0.502	0.500	0.498	0.486	0.466
Band6	0.813	0.829	0.087	0.962	0.986	1	0.983	0.975	0.913	0.499	0.498	0.497	0.487	0.466
Band7	0.813	0.827	0.052	0.948	0.979	0.983	1	0.989	0.941	0.490	0.486	0.481	0.482	0.462
Band8	0.815	0.831	0.044	0.928	0.972	0.975	0.989	1	0.954	0.474	0.466	0.457	0.466	0.448
Band9	0.749	0.762	0.002	0.846	0.919	0.913	0.941	0.954	1	0.401	0.378	0.363	0.366	0.354
Band10	0.370	0.404	0.188	0.553	0.502	0.499	0.490	0.474	0.401	1	0.990	0.980	0.972	0.966
Band11	0.373	0.407	0.193	0.558	0.500	0.498	0.486	0.466	0.378	0.990	1	0.992	0.980	0.971
Band12	0.368	0.402	0.198	0.562	0.498	0.497	0.481	0.457	0.363	0.980	0.992	1	0.969	0.957
Band13	0.385	0.418	0.171	0.544	0.486	0.487	0.482	0.466	0.366	0.972	0.980	0.969	1	0.994
Band14	0.365	0.399	0.178	0.525	0.466	0.466	0.462	0.448	0.354	0.966	0.971	0.957	0.994	1

As can be seen in Table 1, an extremely low correlation (<0.1) has been calculated between the Band3N and the rest of the ASTER Bands. This is justified by that vegetation appears very different at near infrared, visible and short-wave infrared wavelengths. More particularly, because vegetation highly reflects the electromagnetic radiation at near infrared, vegetated areas are highlighted in bright tones in ASTER Band 3N image. On the other hand, vegetation appears relatively dark in the visible and SWIR.

The low correlation values (<0.4) observed between the thermal (Bands 10-14) and the VNIR & SWIR Bands, are easy to interpret considering the fact that the thermal infrared spectrum provides radiant temperature information for the surface materials while the VNIR and SWIR data are correlated to the absorption/reflectance properties of the surface targets.

Along these lines, the Principal Component Analysis has been computed using two different image groups. The first choice has been based on using the three visible-near infrared bands (Bands 1, 2

and 3N) and the six short-wave infrared bands (Bands 4, 5, 6, 7, 8 and 9). Similarly, the second group of image data has used only the five thermal infrared bands (Bands 10, 11, 12, 13, 14).

Band loadings in the range of -1 to +1 have also been computed. These values provide a qualitative as well as a quantitative measure of the relative contribution of an original band onto the corresponding PC image (33).

The vegetation index image

The Normalized Difference Vegetation Index image, i.e.,

$$NDVI = \frac{Band\,3N - Band\,2}{Band\,3N + Band\,2}$$

has been generated to identify differences in the vegetation coverage. The idea has been based on the characteristic and different properties of the spectral response of vegetation in Band 3N (0.78 - 0.86 μm), and Band 2 (0.63 - 0.69 μm). The low reflectance of sun radiation by vegetation in the red region of the electromagnetic spectrum (Band 2) is contrasted to the high reflectance in the near-infrared (Band 3N), by subtracting the two bands (ratio numerator). *NDVI* values range from -1 to 1. In the vegetation index image that was produced, vegetation exhibits positive digital numbers, while clouds and water yield negative values. On the other hand, rocks and soils which typically have roughly equal reflectance in the visible and near-infrared, give values close to zero. To highlight only the vegetation patterns, the techniques of thresholding and classification have been performed. In particular, positive digital numbers have been divided into 10 distinct classes, while negative and zero values have been left out.

False Colour Composite images

A False Colour Composite (FCC) image is an effective means for visual interpretation of multi-spectral imagery. This is because the human eye is more sensitive to colour than greyscale brightness variations (34) and thus interpretation is easier. In order to generate RGB (red-green-blue) composites associated with both high spatial and spectral information, several combinations have been tested mainly between Bands 1, 2 and 3N and the first-order PC images (i.e., PC1 and PC2) of both datasets processed. An effort to produce RGB composites using bands that are totally un-correlated to each other was the main purpose at this stage.

Digital Elevation Model

At the second phase of this investigation, standard GIS techniques have been carried out to help in the evaluation of the lineaments detected on the processed images, as potential faults. Compared to two-dimensional satellite data, a Digital Elevation Model (DEM) has the advantage of representing the vertical extension of the earth's surface by assigning height values for every pixel. The use of DEM has a marked interest for geological mapping especially for highly vegetated terrains and urban areas (35).

In this work, a DEM of 20 m × 20 m spatial resolution and vertical accuracy of ±7 m has been used for the three-dimensional representation of the terrain. The product had been produced using SPOT-4 stereo-pair images and was available in GGRS87, i.e. the same spatial frame of reference used for ASTER bands.

Several DEM products, such as the shaded relief, maps of slope and aspect have been calculated for the identification of faults. For example, a steep slope of the terrain would most likely be a fault scarp. An aspect-slope map would simultaneously show the aspect (the down-slope direction) and degree (steepness) of terrain slope. High slopes and their associated aspects might mark a fault line.

Aspect categories presented in Figure 2, have been depicted using different hues (for example red, orange and yellow) whereas the degree of slope has been represented with saturation, so that steeper slopes appear bright on the image. The method and colouring presentation was based on the Moellering and Kimerling aspect colour scheme (36).
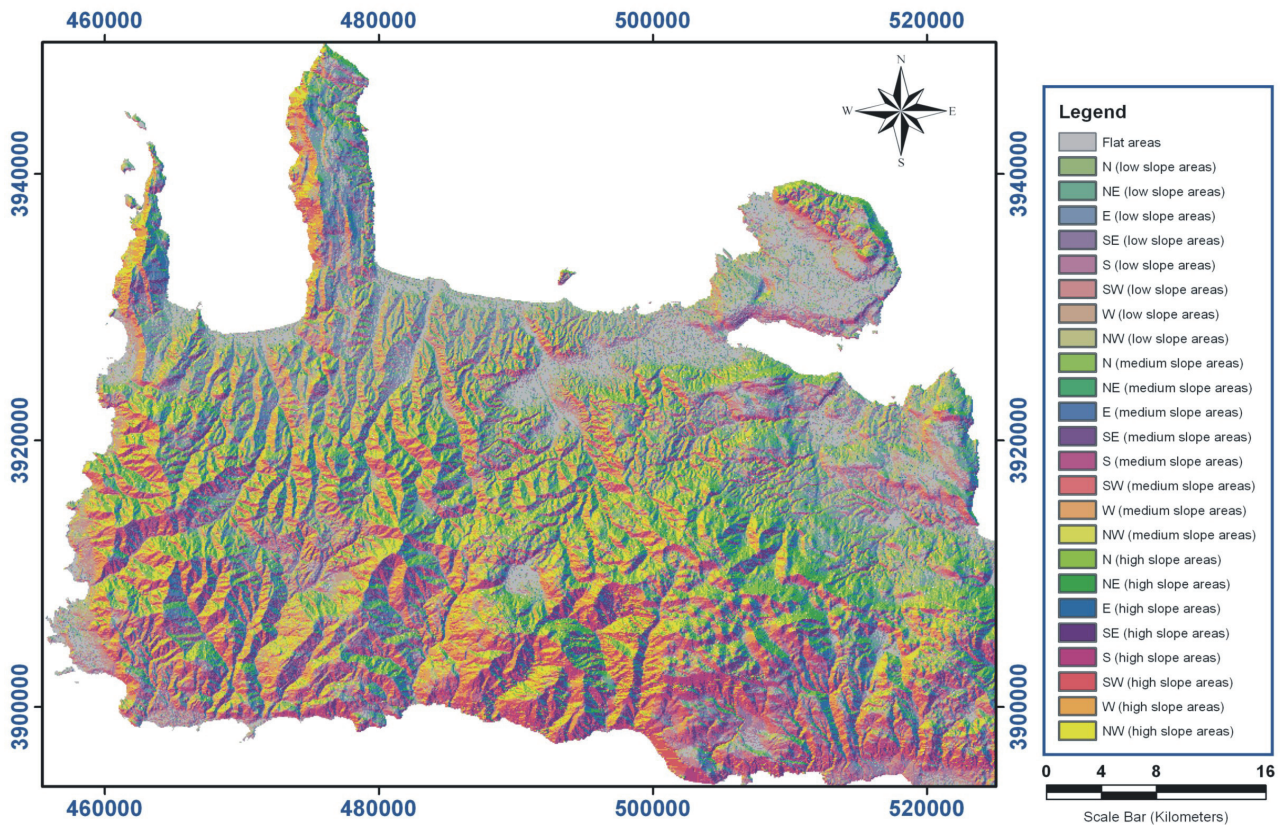
Figure 2: The aspect-slope map of the area. Flat areas are depicted in grey. The rest of the area is divided into 24 classes grouped in three main categories: 1) Low slope areas; 2) medium slope areas, and 3) high slope areas. Each of these categories is divided in eight different aspects (N, NE, E, SE, S, SW, W, NW). The steeper the slope (high slope areas in the legend) the brighter it appears.

Evaluation of lineaments as potential faults

Any linear or curvilinear features observed on the processed ASTER multispectral image that might be related to potential increased soil moisture concentration or vegetation alignments have been digitized. Auxiliary data, such as:

1) the geological maps published by the Institute of Geology and Mineral Exploration (IGME) at scales 1:200 000 and 1:50 000;

2) the drainage network, published by the Hellenic Military Geographical Service (HMGS) at a scale of 1:50 000; and

3) the DEM products, have been inserted into a geographical information system for the evaluation of the lineaments detected, as potential faults.

A detailed structural geological investigation was beyond the scope of this work. Our interpretation was limited to macro-lineaments detected that coincided with:

a) steep slopes (>30°) and straight valley segments extracted from the DEM and its products

b) sudden shifts of drainage courses

c) tectonic contacts between geological formations. Because the geology of the area is characterized by a pile of nappes, several lineaments were associated with tectonic contacts.

RESULTS

The most important results derived from this work are presented below.

Principal Component Analysis

It has been found that almost 90% of the total scene variance has been encompassed in the first two Principal Component images prepared for the first group of data, i.e., PC1 - VNIR & SWIR and

PC2 – VNIR & SWIR (Figures 3a and b, respectively). Instead of analysing the nine original bands, one could safely use these two Principal Component images without significant loss of information. Despite the fact that the second Principal Component image, PC2 – VNIR & SWIR accounted for merely 8% of the total scene variance (Figure 3b), it was of particular interest.
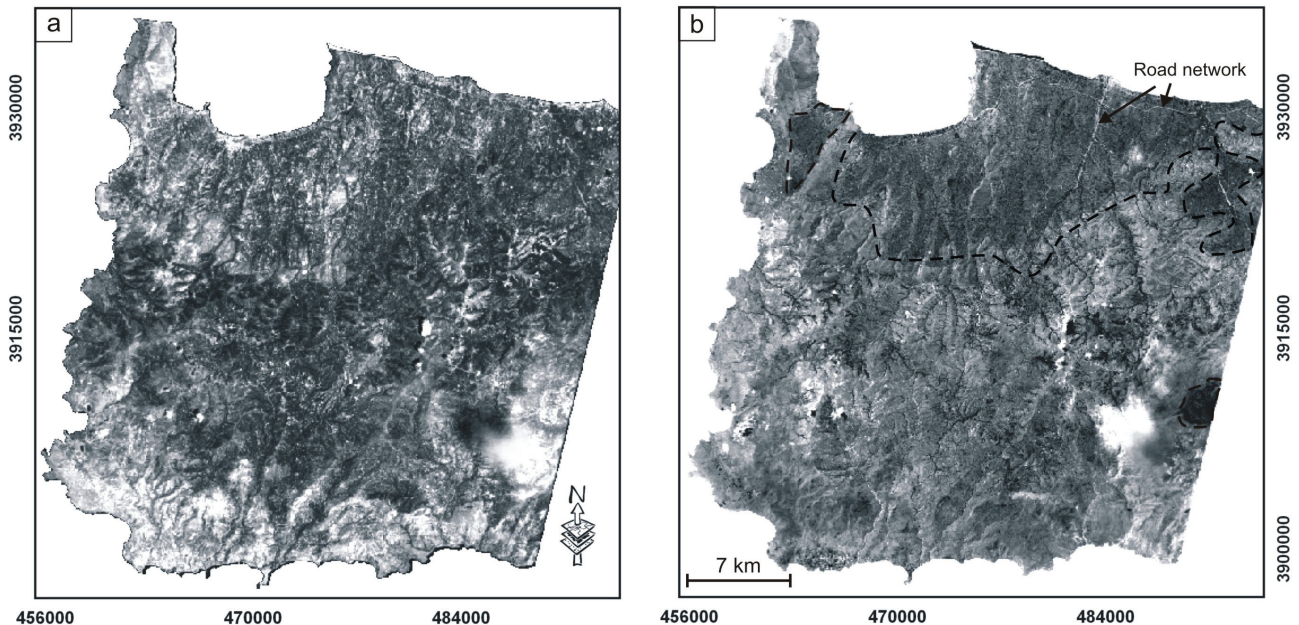
Figure 3: (a) The first Principal Component image for the VNIR and SWIR bands. In terms of ana-lyzing the spectral properties of the surface materials, it is not easy to trace back the potential structural origin of lineaments on this PC1-VNIR&SWIR. This is because it is a weighted sum of the visible and SWIR spectral characteristics of the targets. (b) The second Principal Component image. The Neogene formations are illustrated in dark tones of grey and are clearly distinguished from the surrounding open area. The road network is also highlighted in light tones (black arrows to the NE part of the area).

Band loadings indicated that the information compressed in this PC2 – VNIR & SWIR image originated mostly from the near infrared band (i.e., band 3N) and was therefore highly correlated to vegetation information. In particular, the negative loading calculated (~ -0.9) could justify the appearance of green (healthy) vegetation in relatively dark tones.

Brightness variations demonstrated in Figure 3b and Figure 4 could also be used as indices of different underlying lithologies and/or soil conditions. The Neogene sediments, for example, depicted in relatively dark tones of grey, were readily distinguished from the geological formations of the surrounding, sparse-vegetated area (see Figure 1b for comparison). Note also that the road network has been well demonstrated in bright pixels on this particular PC2 – VNIR & SWIR image. Consequently, lineaments related to roads could be easily excluded at the last phase of this analysis.

Furthermore, comparing the lineaments enhanced in PC2 – VNIR & SWIR product with the geological map of IGME (Figure 1b), it could be seen that several lineaments were related to tectonic contacts between formations. Some indicative examples are locations No.1, 2, 3, and 4 as presented in Figure 4. For example, lineament at location No. 1 represents a tectonic contact between the Limestones of Pindos unit, depicted as pixels of variable greyness, and the Neogene deposits, shown as dark pixels. Other distinct tectonic contacts between the Limestones of Gavrovo-Tripolitza unit (presented in intermediate tones of grey) and the Marly Limestones of Miocene, shown in comparatively darker pixels are indicated at locations No. 2, 3 and 4 in Figure 4.

On the other hand, the first Principal Component image prepared for the thermal infrared bands (i.e., PC1-TIR) contained 98% of the variation of the five original ASTER TIR bands. This is a significant compression of data in this first Principal Component. Despite the low spatial resolution in

the TIR band, numerous lineaments have been detected (Figure 5). Comparison with the topographical map of the area has shown that most of the lineaments enhanced corresponded to the drainage lines. However, several dark linear features could also be spotted (some examples are indicated by the yellow arrows in Figure 5) that did not coincide with the drainage and might therefore have a relevance to tectonics.
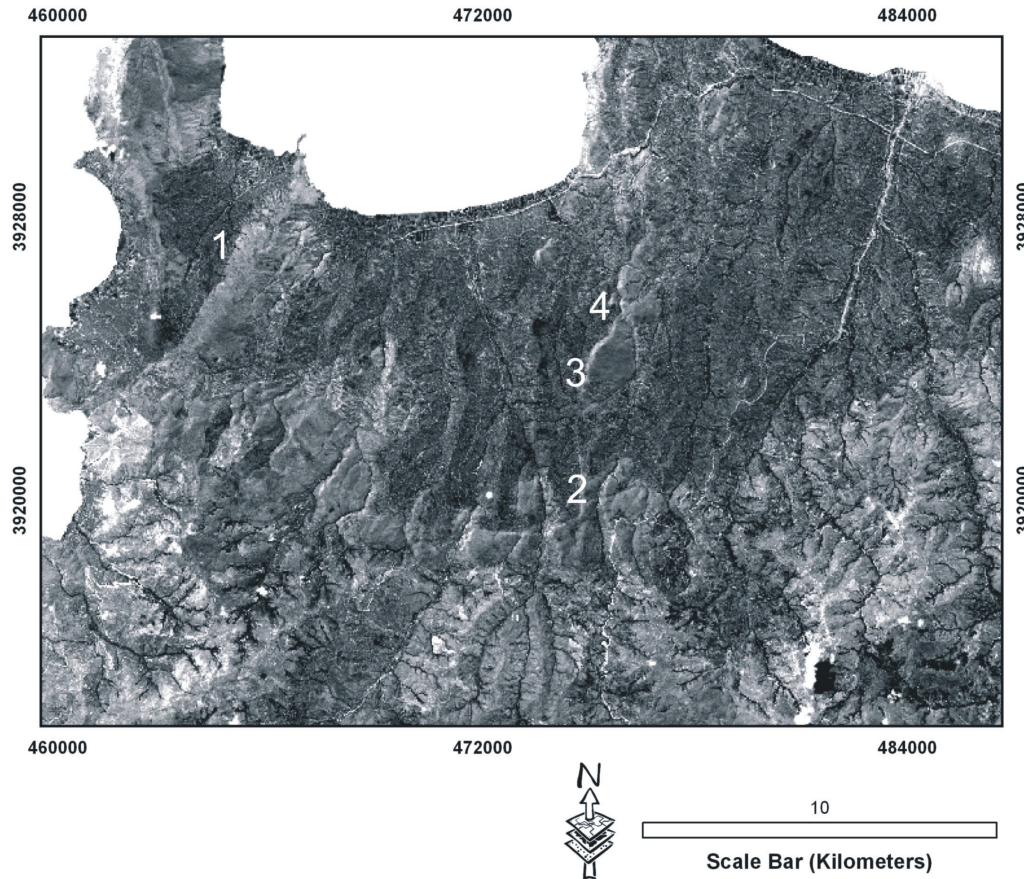
Figure 4: Image showing the second Principal Component image for the VNIR and SWIR bands (i.e., PC2-VNIR&SWIR). The Neogene sediments are characterized by relatively dark brightness values. Tectonic contacts between geological formations were established at locations 1 - 4 because of their distinct linear shape and tonal contrast with the surrounding area.

To further enhance lineaments related to soil moisture content, the PC1-TIR image was integrated with the near infrared data (i.e., ASTER Band 3N). In both images, PC1-TIR and Band 3N, soil moisture is represented by relatively dark pixels. This has been justified earlier on because 1) wet soils relate to low radiant temperature values on the TIR bands; and 2) water absorbs radiation in the near-infrared and consequently moist soil appears darker than dry soil.

Thus, linkage and overlay of the two image datasets (i.e., the PC1-TIR image and ASTER Band 3N), within a GIS environment, amplified the contrast between potential wet and dry soils (Figure 6). Lineaments depicted with dark pixels in Figure 6 have a higher probability to be related to increased soil moisture content.

The drainage was particularly enhanced on this "combined" image in Figure 6, mainly because of vegetation growth along the rivers (bright tones of grey). It could be thus used to analyze the relation between lineaments and drainage pattern. Accordingly, the lineaments spotted at locations No.1-11 have been evaluated as potential zones of structural weakness. These lineaments are not coincident with drainage lines while their linearity, large extent (see for example, lineaments 5-7) and in some case their relation with sudden shifts of the rivers courses, could be attributed to failure of the crust.
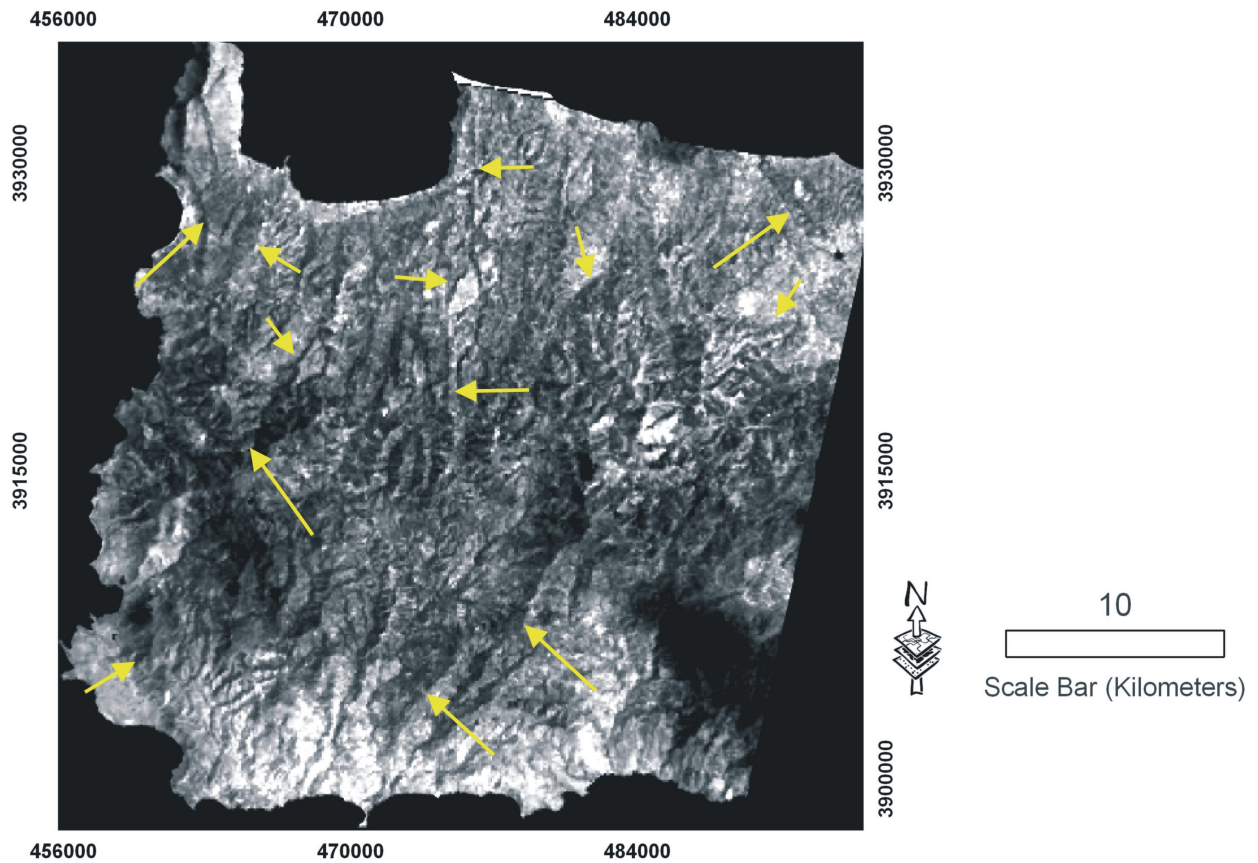
Figure 5: The PC1-TIR image showing linear features of low radiant temperature (dark brightness values). Despite the low spatial resolution, this particular image demonstrates numerous lineaments possibly related to increased soil moisture (yellow arrows).
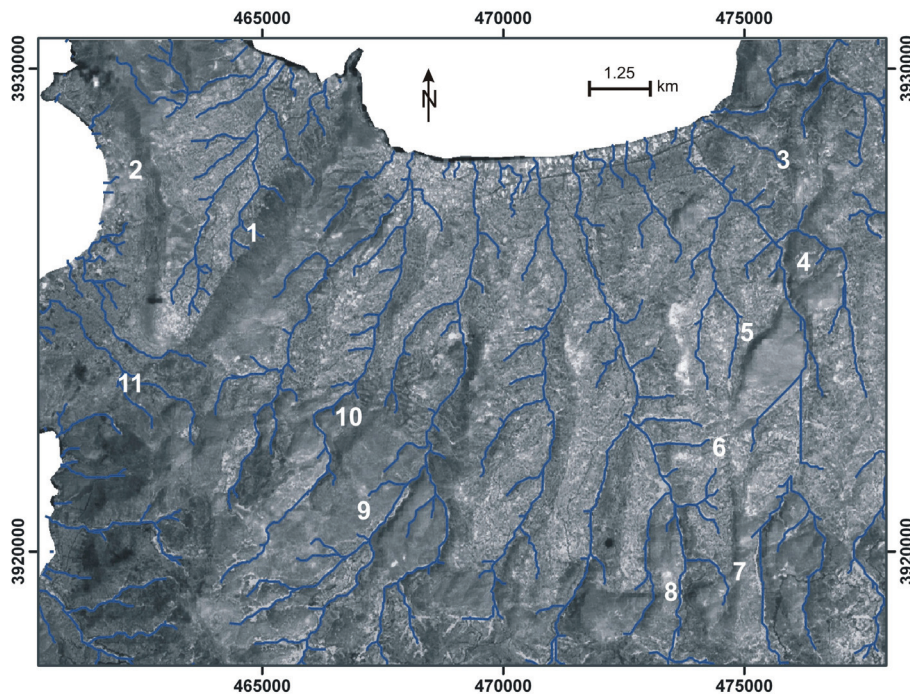

Figure 6: Overlay of the PC1-TIR component image and the near infrared-red image (ASTER Band 3N). Increased soil moisture appears in relatively dark brightness values. The solid blue lines represent the drainage lines digitized from the topographical maps of the area. Lineaments at locations No.1-11 have been evaluated as potential faults that control the drainage system of the area.

The vegetation index image and the drainage network

The drainage of the area and the classified vegetation index image (Figure 7a) have been examined and compared. As mentioned earlier on, the vegetation pattern is extensively coincident with the drainage network. This could be justified by that, in Western Crete, the majority of the waterways are mainly constituted by intermittent streams which encourage the development of hydric plants.

Linearity of vegetation has been examined in relation to the course followed by the streams. Lineaments that coincided with long linear drainage lines, as well as sudden river bends have been attributed to potential fault zones. Figure 7b (Google Earth image) presents an indicative example of vegetation alignment along a fault zone (short dotted line in Figure 7a-inset b). This particular lineament is also related with a sudden course shift of a, most likely, inactive stream channel.
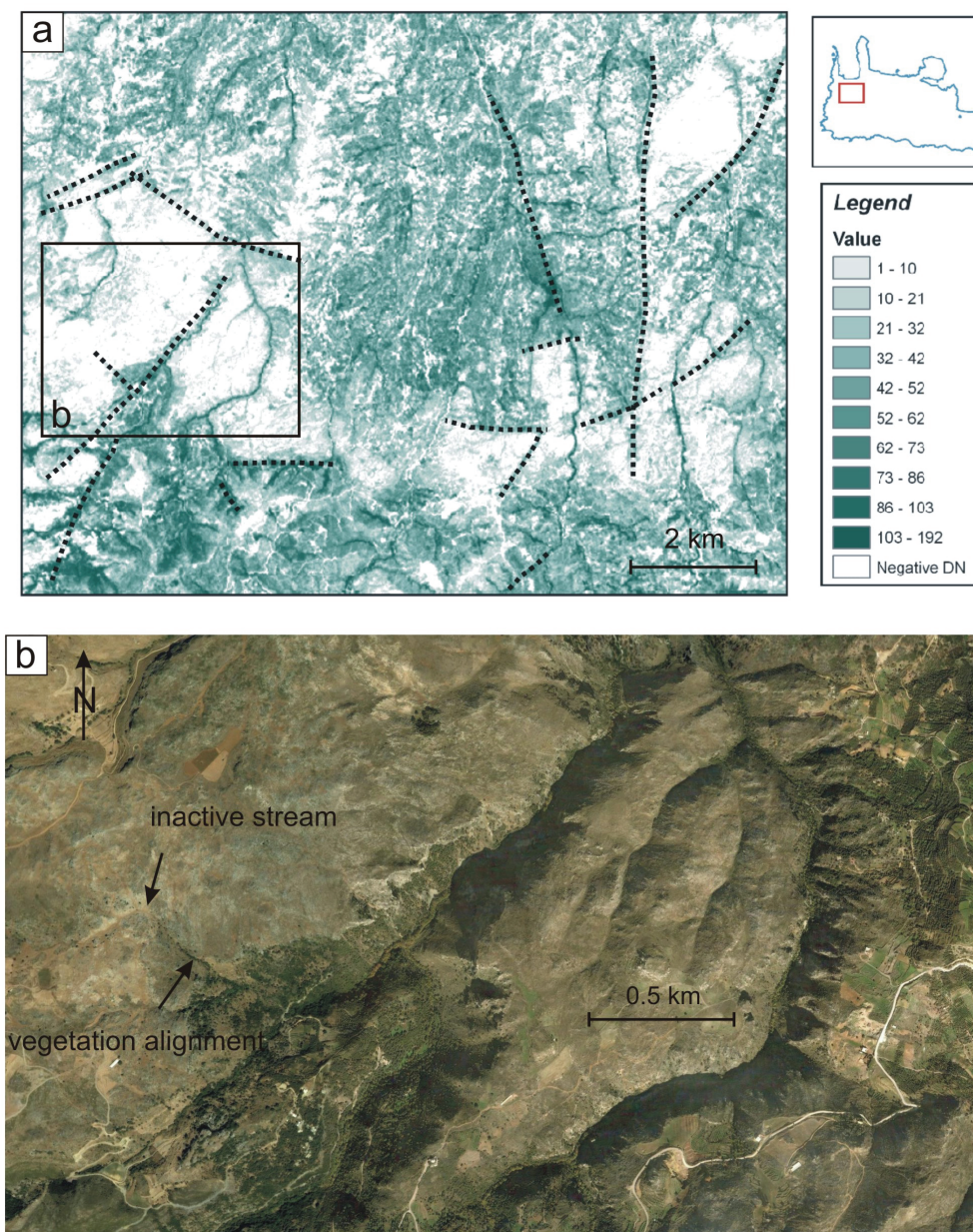

Figure 7: (a) Part of the segmented vegetation index image. The dotted lines refer to vegetation that is mainly but not exclusively developed along rivers. The higher values (for example the last two classes) represent very green areas (i.e., healthy vegetation retaining relatively high moisture content). (b) Google Earth image, illustrating a typical example of vegetation growth along a fault zone. The stream course seems to be also controlled by the fault.

The False Colour Composite image

Compression of the information contained in the 14 original bands in only one RGB composite image has been achieved by assigning PC1-TIR image to red, PC1-VNIR&SWIR image to green and PC2-VNIR & SWIR image to blue. Note that each of these three Principal Component images was totally uncorrelated to each other. Figure 8 presents this RGB combination image superimposed over the shaded relief of the area. Numerous lineaments can be spotted on it based on colour variations. The shadowing effect of the DEM product used in the background has enhanced the land relief.
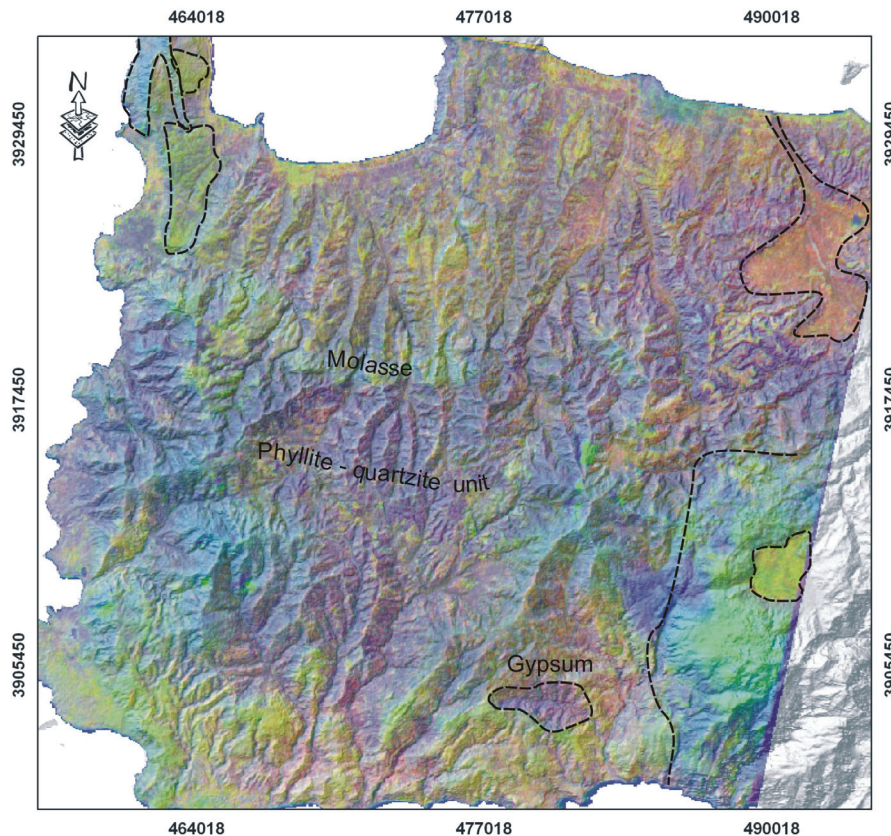
Figure 8: The three-band False Colour Composite image superimposed over the shaded relief of the area. Here colours are represented as PC1-TIR=Red, PC1 – VNIR & SWIR=Green and PC2 – VNIR & SWIR=Blue. The spectral information initially encompassed in the 14 original ASTER bands is compressed in a single RGB composite. Despite the fact that PC images used to form RGB composites are not easy to interpret, several geological formations are well delineated in this product.

A detailed geological mapping was beyond the scope of this study. Nonetheless, studying the 1: 200 000 scale geological map (Figure 1b), it is clear that the colour variations in Figure 8 could be associated with the boundaries of specific geological formations. More particularly:

- the Phyllite-Quartzite unit is represented in bluish to purple colour variations,

- the alluvium deposits, in the NE part of the image, are highlighted in orange tones,

- the Tripolitza unit (see for example the area bounded by dotted lines in the NW peninsula), appears in cyan colour. The sediment deposits in contact to the Tripolitza unit have a characteristic light green-yellow colour.

Along these lines, a map of major lineaments with possible relevance to failure of the crust has been produced. Figure 9a presents the faults previously mapped by IGME at scales 1: 50 000 (black dashed lines) and 1:200 000 (black solid lines). Note that large-scale faults that were established in the framework of EMERIC-CRINNO (Crete Innovative Region) research project (http://www.ims.forth.gr/joint_projects/emeric/emeric-gr.html) have also been incorporated to the 1: 200 000 scale geological map, in Figure 9a.

Figure 9b presents the lineaments detected and attributed to potential faulting in the present work (dark blue solid lines) and their inferred extensions (yellow dotted lines). Locations where limited fieldwork survey verification took place (marked with black dots on Figure 9b), have been established by the Global Positioning System.

There is a general agreement between the macro-scale lineaments detected in this analysis and the faults previously mapped by IGME (1:200 000 scale map) and EMERIC-CRINNO project. Hitherto unmapped extensions of large known faults can be easily traced in the broader area south of "Rokka" and "Kera" and south-west of "Rodopos". These fault zones having similar direction and aspect (see Figure 2 for comparison) seem to be parts of a major failure of the crust along which increased soil moisture content was also detected (Figure 6, lineaments 3-7). Nonetheless, the variations observed between Figure 9a and Figure 9b clearly manifest that fieldwork investigations constitute an indispensable tool for geological mapping.
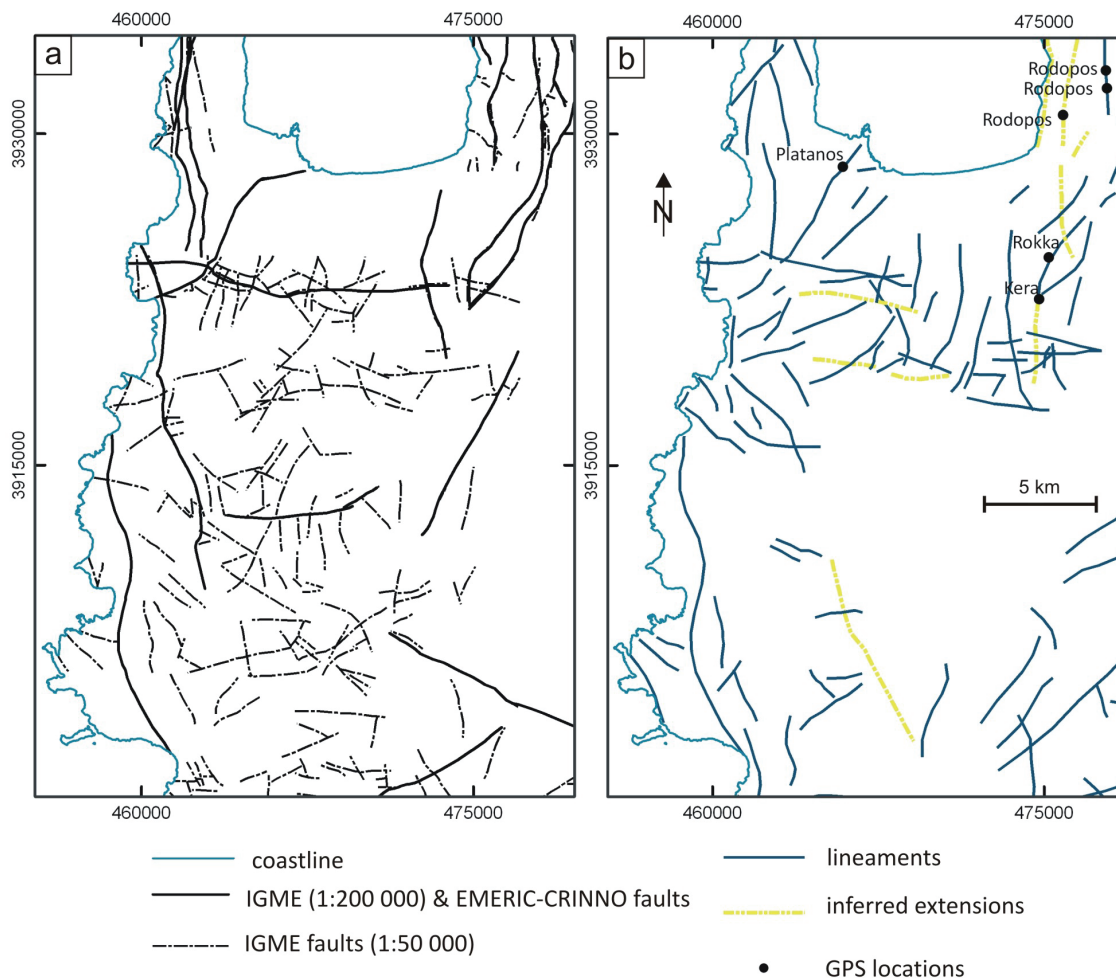

Figure 9: (a) Map of previously verified faults by IGME and EMERIC-CRINNO geological surveys. (b) Map showing the lineaments identified in the present work that might be attributed to failure of the crust. Limited fieldwork locations are also depicted. Especially in the case of macro-lineaments (>8 km) there is a good agreement between the two maps.

DISCUSSION

This work presents an investigation into integrating satellite remote sensing and GIS techniques for detecting lineaments that might be related to faults. A major limitation of processing satellite images for fault mapping is the planar view. However, within a geographic information system, a large amount of data such as DEMs, geological and topographical maps, earth surface parameters, can be linked together and overlain, to eventually analyse extended areas and in a relatively short time.

At the first step, an ASTER multispectral-image has been processed for lineament identification. ASTER data have been successfully used in the past for a variety of geological applications mainly related to mapping rock types and alteration products (37-40). In the field of structural geology the corresponding bibliography is rather limited.

Lineaments could not be easily detected at first, in the raw ASTER data, but only after some image processing had taken place. The two individual PCA approaches that have been applied compressed the information initially contained in the 14 ASTER bands, in fewer components. The first group involved the data from the VNIR and SWIR while the second group involved processing of the five TIR bands. In the first case, PC1 – VNIR & SWIR could be used as an approximation of the albedo giving no specific spectral information on material differentiations. This is justified by that this particular PC image is a weighted sum of all the bands used in the transformation.

As mentioned earlier on, PC2 – VNIR & SWIR image was expressed by a high negative Band 3N loading value. Due to the negative sign, dark tones were attributed to vegetation. However, interpretation of the vegetation index image and a variety of FCC composites produced using the near-infrared data, have shown that these dark patterns were highly correlated to the underlying geology rather than vegetation canopy. The PC2 – VNIR & SWIR image could be therefore used as a reference image for the main geological units (i.e., the Neogene formations, the Pindos and Tripolitza units as well as the lower Phyllite-Quartzite unit). For example, in the NE part of the area in Figure 3b, there is a distinct contrast between the alluvium (dark tones) and the sedimentary rocks of the Phyllite-Quartzite unit (relatively lighter tones).

With reference to the second group of TIR bands, it has been shown that despite the limited spatial resolution of 90m×90m, ASTER TIR bands may provide essential information on the moisture contained in the soil and thus be useful for drainage mapping and potential fault detection. Note that the ASTER data used in this work were acquired in day-time. ASTER TIR day-time acquisitions have been used for several geological applications with varying degrees of success (41,42). However, as noted by Hou and Mauger (2005), day-time temperatures generally mask the surface emissivity properties (43). According to the same authors, the problem could be overcome with the use of ASTER night-TIR data (ASTER NTIR). Nevertheless, ASTER NTIR data are not readily available and arrangements for planned night-time acquisitions should be made first.

PC1-TIR was considered as an image dominated by radiant temperature variations between cooler (dark tones) and warmer targets (light tones). Especially when it was integrated with the near infrared data, lineaments with possible relevance to increased soil moisture content were amplified in dark tones, representing cool radiant temperatures. The drainage extracted from the topographical map of the area has been very helpful in evaluating these dark linear features as potential faults. Specific drainage pattern observations (mainly sudden changes in the river courses) have been a key element in this evaluation.

The classified vegetation index image has contributed in the identification of several vegetation alignments that might also be related to structural weakness of the crust. However, some allowance must be also made for the nature of the footwall rocks, which can exert an important influence on the vegetation patterns observed on the satellite images. The type and permeability of the geological formations are determinant for their moisture retaining capacity and vegetation coverage. For similar investigations in the future, it is suggested to correlate the vegetation patterns with the permeability of underlying rocks. Note however, that when vegetation covers the ground it is difficult to distinguish what lies underneath. The majority of the investigations on mapping faults using remote sensing techniques have been conducted in arid areas (44). Harding and Berghoff (2000) suggested that fault scarps may be revealed under dense vegetation using airborne Lidar mapping technique (45). Nonetheless, vegetation is considered a limiting factor for geological and lithological mapping.

For lineament evaluation as potential faults, attention should be paid regarding the scale of the reference geological map. In this study, the available geological maps at both 1:200 000 and 1:50 000 scales have been used. The first, generalized map at 1:200 000 gave a synoptic view of the main geological units and the main large-scale faults (>8 km). The objective of using the corre-

sponding 1: 50 000 maps (4 map sheets cover the study area) was to evaluate the relatively small-scale lineaments (i.e., extending <5 km in length).

A total of 119 lineaments have been evaluated as potential faults extending from 4-15 km (Figure 9b). There was a quite satisfactory agreement between the macro-lineaments (>8 km) and the faults extracted from IGME map of 1:200 000 scale and EMERIC-CRINNO research project. Lineaments less than 7 km in length have been compared with the corresponding 1:50 000 IGME map. It has been concluded that these lineaments have been mainly enhanced due to the shadowing effect commonly observed on satellite images.

The applied methodology has helped in tracing known large-scale faults at "Rodopos", "Kera", and "Rokka" and infer for their extension under the sediment canopy (yellow dotted lines in Figure 9b). For a more detailed, local geology analysis, higher spatial resolution satellite images could be used instead (for example IKONOS and Quickbird). The trade-off is that a large number of such images should be used to cover the area depicted in one ASTER multi-spectral image. In addition, the IKONOS and Quickbird systems do not cover such a wide spectral range as the one covered by ASTER. Because of both time and financial limitations, processing of other satellite data has not been carried out.

It should be pointed out that image processing techniques have successfully mapped major fault systems around the world extending to hundreds of kilometres (for example the San Andreas in California, the Kunlun in China, the Dead Sea fault). In this work, the longest lineament was detected to the south-western part of the image and amounted to barely 16 km in length. Moreover, in such a complex environment as Crete with piles of nappes and vegetation, mapping faults based only on satellite imagery is not recommended. Integration with data from multiple sources and fieldwork investigations is strongly suggested.

CONCLUSIONS

There are geomorphology and drainage patterns that control the structural geology and are recognizable on satellite images and digital topography. ASTER multi-spectral images could be used for the identification of lineaments possibly related to faults but under certain conditions.

It has been shown that especially near infrared and thermal infrared data might be helpful in identifying linear patterns of vegetation and soil moisture concentration. However, it is difficult to distinguish the structural origin of a lineament relying only on satellite images.

The evaluation of lineaments detected can be easily performed in a GIS environment based on distinguished surface characteristics that could manifest a fault zone (for example topography and drainage). In this work, the DEM and its derived products have been the most important source for identifying lineaments that are potential faults as these commonly relate to straight valley segments and steep slopes.

The presented methodology could be used as a preliminary step to spot potential faults that have to be investigated in the field. The extent and potential interrelation between individually mapped faults (for example at "Rodopos", "Roka" and "Kera") not easily recognized at close range due to vegetation overgrowth, may be easier identified and mapped on satellite imagery. Both field and remote sensing methods should be combined to correct and update existing information on geological maps. Note however that as soon as vegetation covers the terrain it is difficult to extract information about the underlying rock or soil characteristics and/or reveal lineaments of structural origin.

ACKNOWLEDGEMENTS

REFERENCES

1   Colwell R N, F T Ulaby, D S Simonett, J E Estes & G A Thorley (Eds.), 1983. <u>Manual of Remote Sensing, vol. 2: Interpretation and Applications</u>, 2nd ed., American Society of Photogrammetry and Remote Sensing, 1728-1755 (Sheridan Press) 2440 pp.

2   Drury S A, 1987. <u>Image Interpretation in Geology</u>, 66-148 (Kluwer Academic Publishers) 296 pp.

3   Cracknell A P & L Hayes, 1991. <u>Introduction to Remote Sensing</u> (Taylor & Francis Press) 304 pp.

4   O'Leary D W, J D Friedman & H A Pohn, 1976. Lineament, linear, lineation: some proposed new definitions for old terms. <u>GSA Bulletin</u>, 87(10): 1463-1469

5   Miller V C, 1961. <u>Photogeology</u> (McGraw-Hill) 248 pp.

6   Nama E E, 2004. Lineament detection on Mount Cameroon during the 1999 volcanic eruptions using Landsat ETM. <u>International Journal of Remote Sensing</u>, 25: 501-510

7   Ali S A & S Pirasteh, 2004. Geological applications of Landsat enhanced thematic mapper (ETM) data and geographic information system (GIS): mapping and structural interpretation in south-west Iran, Zagros structural belt. <u>International Journal of Remote Sensing</u>, 25: 4715-4727

8   Kenea N H, 1997. Improved geological mapping using Landsat TM data, Southern Red Sea Hills, Sudan: PC and HIS decorrelation stretching. <u>International Journal of Remote Sensing</u>, 18: 1233-1244

9   Suzen M L & V Toprak, 1998. Filtering of satellite images in geological lineament analyses: an application to a fault zone in Central Turkey. <u>International Journal of Remote Sensing</u>, 19: 1101-1114

10 Heddi M, D J Eastaff & J Petch, 1999. Relationships between tectonic and geomorphological linear features in the Guadix-Basa basin, Southern Spain. <u>Earth Surface Process and Landforms</u>, 24: 931-942

11 Semere S & W Ghebread, 2006. Lineament characterization and their tectonic significance using Landsat TM data and field studies in the central highlands of Eritrea. <u>Journal of African Earth Sciences</u>, 46: 371-378, DOI: 10.1016/j.jafrearsci.2006.06.007

12 Marghany M, M Hashim & S Mansor, 2009. Geologic mapping of United Arab Emirates using multispectral remotely sensed data. <u>American Journal of Engineering and Applied Sciences</u>, 2(2): 476-480

13 Maged M & H Mazlan, 2010. Lineament mapping using multispectral remote sensing satellite data. <u>Research Journal of Applied Sciences</u>, 5(2): 126-130, DOI: 10.3923/rjasci.2010.126.130

14 Stefouli M & H Osmaston, 1986. The analysis of linear geologic features on Landsat images of Crete. <u>Journal of the British Interplanetary Society</u>, 39: 546-551

15 Adediran A O, I Parcharidis, M Poscolieri & K Pavlopoulos, 2004. Computer-assisted discrimination of morphological units on north-central Crete (Greece) by applying multivariate statistics to local relief gradients. <u>Geomorphology</u>, 58: 357-370

16 Sarris A, S Karakoudis, C H Vidaki & P Soupios, 2005. Study of the morphological attributes of Crete through the use of remote sensing techniques. <u>International Association of Mechanical Engineers (IASME) Transactions</u>, 6 (2): 1043-1051

17 Abrams M, S Hook & B Ramachandran, 2000. ASTER User Handbook, Version 2 (Jet Propulsion Lab, NASA) 135 pp.

18 Fasoulas C, 1995. <u>Kinematics and Deformation of the Nappes in Central Crete, Greece.</u> PhD Thesis, Aristotle University of Thessaloniki, Thessaloniki, Greece

19 Fytrolakis N, 1980. <u>The Geology of Crete Island.</u> PhD Thesis, National Technical University of Athens

20 Richter D, J Krahl, G Kaufmann, H Kozur, O Förster & F Heinritzi, 1983. Neue Daten zur Bi-
    ostratigraphie und zur tektonischen Lagerung der Phyllit-Gruppe und der Trypali-Gruppe auf
    der Insel Kreta (Griechenland). Geologische Rundschau, 72: 1147-1166

21 Seidel E & T Theye, 1993. High-pressure/low-temperature metamorphism in the external Hel-
    lenides (Crete, Peloponnese). Bulletin of the Geological Society of Greece, 28: 49-55

22 Fassoulas C, A Kilias & D Mountrakis, 1994. Post-nappe stacking extension and exhumation
    of the HP/LT rocks in the island of Crete, Greece. Tectonics, 13: 127-138

23 Kilias A, C Fassoulas & D Mountrakis, 1994. Tertiary extension of continental crust and uplift
    of Psiloritis metamorphic core complex in the central part of the Hellenic arc, Crete, Greece.
    Geologische Rundschau, 83: 417-430

24 Aubouin J & J Dercourt, 1965. Sur la géologie de l'Égée: Regard sur la Crete (Greece). Bulle-
    tin de la Société Géologique de France, VII: 787-821

25 Frydas D, H Keupp & S Bellas, 1999. Biostratigraphical research in Late Neogene marine de-
    posits of the Chania province, western Crete, Greece, Berliner Geowissenschaftliche Abhan-
    dlungen E, 30: 55-67

26 Ten Veen J H & P T Meijer, 1999. Late Miocene to recent tectonic evolution of Crete (Greece):
    geological observations and model analysis. Tectonophysics, 298: 191-208

27 Fasoulas C, 1999. The structural evolution of central Crete: insight into the tectonic evolution
    of the South Aegean. Journal of Geodynamics, 27: 23-43

28 Crippen R E, 1989. Development of Remote Sensing Techniques for the Investigation of Neo-
    tectonic Activity, Eastern Transverse Ranges and Vicinity, Southern California. PhD Disserta-
    tion, Univ. of California, Santa Barbara

29 Gillespie A, S Rokugawa, T Matsunaga, J S Cothern, S Hook & A B Kahle, 1998. A tempera-
    ture and emissivity separation algorithm for advanced spaceborne thermal emission and re-
    flection radiometer (ASTER) images. IEEE Transactions of Geoscience and Remote Sensing,
    36: 1113-1126

30 Johnson R A & D W Wichern, 2002. Applied Multivariate Statistical Analysis, 5th ed. (Prentice Hall)
    767 pp.

31 Shuichi M, 2002. Regional lineament analysis and alteration mineral mapping for intrusive-
    related copper exploration in the Myanmar central volcanic belt. Asian Conference on Remote
    Sensing 2002 (Kathmandu, Nepal)
    http:/www.gisdevelopment.net/aars/acrs/2002/pos3/039.pdf (last date accessed: 13 March 2011)

32 Annoni A, C Luzet, E Gubler & J Ihde, 2001. Map Projections for Europe. European Commis-
    sion, Joint SResearch Centre ISPRA, EUR 20120 EN, 132 pp.
    http://www.ec-gis.org/sdi/publist/pdfs/annoni-etal2003eur.pdf (last date accessed: 13 March 2011)

33 Palluconi F, A B Kahle, G Hoover & H E Conel, 1990. The spectral emissivity of prairie and
    pasture grasses at Konza Prairie, Kansas, Proceedings of the American Meteorological Soci-
    ety, Symposium on FIFE, 77-78

34 Gonzalez R C, R E Woods & S L Eddins, 2004. Digital Image Processing (Prentice Hall) 976
    pp.

35 Cirés J, J Marturià, A de Paz, J Casanovas & A Lleopart, 1997. Digital elevation models, a
    useful tool for geological mapping. Some examples from Catalonia. Institut Cartogràfic de Ca-
    talunya, Second Congress on Regional Geological Cartography and Information Systems,
    Barcelona, Spain
    http://www.icc.cat/content/download/3613/11738/file/digital_elevation_models.pdf (last date
    accessed: 13 March 2011)

36 Moellering H & A J Kimerling, 1990. A new digital slope-aspect display process. Cartography and Geographic Information Systems, 17(2): 151-159

37 Stamoulis V & P Rogers, 2003. Geological mapping for mineral exploration using ASTER data. MESA Journal, 30:16-19
    https://egate.pir.sa.gov.au/webbasis/WebtopEw/ws/samref/gui/image/DDD/MESAJ030.pdf

38 Yamaguchi Y & C Naito, 2003. Spectrail indices for lithologic discrimination and mapping by using the ASTER SWIR bands. International Journal of Remote Sensing, 24(22): 4311-4323

39 Rowan LC & JC Mars, 2003. Lithologic mapping in the Mountain Pass, California, area using Advanced Spaceborne Emission and Reflection Radiometer (ASTER) data. Remote Sensing of Environment, 82: 350-366

40 Rowan LC, RG Schmidt & JC Mars, 2006. Distribution of hydrothermally altered rocks in the Reko Diq, Pakistan mineralized area based on spectral analysis of ASTER data. Remote Sensing of Environment, 104(1): 74-87

41 Stamoulis V, 2006. ASTER night-time thermal infrared data: interpreting subsurface features from high resolution data. MESA Journal, 43: 36-43
    https://egate.pir.sa.gov.au/webbasis/WebtopEw/ws/samref/gui/image/DDD/MESAJ043.pdf

42 Elena M, 2005. Thermal Infrared ASTER Observations of Faults in Southern California. EOS Trans. AGU, 86(52), Fall Meet. Suppl. abstract #T51B-1346

43 Hou B & A J Mauger, 2005. How well does remote sensing aid palaeochannel identification? An example from the Harris Greenstone Belt. MESA Journal, 38:46-52
    https://egate.pir.sa.gov.au/webbasis/WebtopEw/ws/samref/gui/image/DDD/MESAJ038.pdf

44 Gomez C, C Delacourt, P Allemand, P Ledru & R Wackerle, 2005. Using ASTER remote sensing data set for geological mapping, in Namibia. Physics and Chemistry of the Earth, 30: 97–108

45 Harding D J & G S Berghoff, 2000. Fault scarp detection beneath dense vegetation cover: airborne Lidar mapping of the Seattle fault zone, Bainbridge island, Washington state. Proceedings of the American Society of Photogrammetry and Remote Sensing, Annual Conference, Washington, DC, 9 pp.
    http://ntrs.nasa.gov/archive/nasa/casi.ntrs.nasa.gov/20000060844_2000076193.pdf (last date accessed: 13 March 2011)